Artificial Intelligence In Medicine 108 (2020) 101940

Contents lists available at ScienceDirect

Artificial Intelligence In Medicine

journal homepage: www.elsevier.com/locate/artmed

Position Paper

Identification of Alzheimer's disease based on wavelet transformation energy feature of the structural MRI image and NN classifier

Jinwang Feng [a], Shao-Wu Zhang [a,*], Luonan Chen [a,b,c,*], Alzheimer's Disease Neuroimaging Initiative (ADNI)

[a] Key Laboratory of Information Fusion Technology of Ministry of Education, School of Automation, Northwestern Polytechnical University, Xi'an 710072, China
[b] Key Laboratory of Systems Biology, Shanghai Institute of Biochemistry and Cell Biology, Center for Excellence in Molecular Cell Science, Chinese Academy Science, Shanghai 200031, China
[c] Key Laboratory of Systems Biology, Hangzhou Institute for Advanced Study, University of Chinese Academy of Sciences, Chinese Academy of Sciences, Hangzhou 310024, China

ARTICLE INFO

Keywords:
Alzheimer's disease
Image classification
Wavelet transformation
Feature extraction
Energy feature
MSC:
00-01
99-00

ABSTRACT

Alzheimer's disease (AD) is now difficult to be identified for clinicians, especially, at its prodromal stage, mild cognitive impairment (MCI), because of no obvious clinical symptom and few impacts on daily life at this phase. In addition, energy distribution differences of brain atrophies reflected in structural magnetic resonance imaging (sMRI) images between MCI patients and older healthy controls (HC) are minimal and subtle, which are difficult to be captured by the spatial analysis. In this study, we propose a novel method (namely AD-WTEF) to identify AD and MCI patients from HC subjects by extracting the wavelet transformation energy feature (WTEF) of the sMRI image. AD-WTEF firstly transforms each scan of the preprocessed sMRI image by wavelet to obtain its directional subbands with the same size at different transformation levels. And then, based on the anatomical automatic labeling (AAL) atlas, AD-WTEF constructs a new brain mask to segment the subbands at the same direction and transformation level into different energy regions of interest (EROIs). Thirdly, by averaging coefficients in an EROI, AD-WTEF gets an energy feature, following that energy features of different EROIs are connected to form an energy feature vector for describing the subbands at the same direction and transformation level. As a result, these energy feature vectors are further concatenated to be a WTEF of the sMRI image. Finally, the nearest neighbor (NN) classifier is selected and used for AD identification. Compared with other seven state-of-the-art methods, our AD-WTEF can effectively identify AD patients using the subtle energy distribution differences of sMRI images. Furthermore, experimental results indicate that our AD-WTEF can also find important brain ROIs related to AD.

1. Introduction

Alzheimer's disease (AD), as a main cause of dementia, is a progressive neurodegenerative disease characterized by many symptoms such as memory loss and cognitive decline, which has received a lot of attentions from medical field and academia [1–3]. As the major form of dementia, AD had affected 26.6 million people worldwide in 2006 and has been predicted to affect 1 in 85 people by 2050 [4,5]. The main reason is that the early symptoms do not affect the normal daily activities, so few attentions are put on to the early stage of this disease. However, along with the development of neurodegeneration, a person with AD will not deal with his daily life and not return health again until to death. Taking the year 2010 as an example, according to the 2010 World Alzheimer Report, there are an estimated 35.6 million people worldwide living with dementia at a total cost of more than US$600 billion in 2010 [6,7]. Hence, early diagnosis of AD based on clinical test and magnetic resonance imaging (MRI) is emergently needed to delay or stop the progression of this disease.

According to the type of features extracted from the sMRI image, the existing works about AD identification can be roughly categorized into the spatial domain-based [8–11] and the transformation domain-based [12,13]. For the spatial domain-based method, features can be easily extracted by analyzing structures of the sMRI image [14], for example, the simplest voxel-based features consist in directly using the voxels of

* Corresponding authors.
E-mail addresses: zhangsw@nwpu.edu.cn (S.-W. Zhang), lnchen@sibs.ac.cn (L. Chen).

https://doi.org/10.1016/j.artmed.2020.101940
Received 8 January 2020; Received in revised form 1 July 2020; Accepted 7 August 2020
Available online 11 August 2020

the tissue probability maps [15–20]. Though some techniques are proposed to reduce the impacts of noisy and dimensionality such as smoothing, downsampling, feature selection, and automated anatomical labeling (AAL) atlas [21–25], problems of the high dimensionality and noise are only alleviated to a certain extent. For the transformation domain-based method, images are decomposed or transformed into the frequency domain to obtain subbands at different directions and transformation levels using the transformation tools such as wavelet, courtlet, and shearlet [26,27], and then energy features are obtained by averaging coefficients contained in these subbands. Hence an image is represented by a subband energy feature vector or mapping in performing classification. However, impacts of the noise and dimensionality can be only reduced at a relatively low decomposition level and making a appropriate segmentation to the subband is also difficult in extracting energy features [28–30]. So, challenges of this kind of method are how to extract powerful energy features at a low decomposition level and how to reasonably segment subbands for capturing energy distributions of the subband.

Artificial intelligence (AI) had been recognised as a potential and powerful tool to predict disease outcome in many clinical situations many years ago [31,32]. In the field of machine learning, convolutional neural networks, as an outstanding branch of deep learning applications, have earned major attention in medical image analysis domain [33–36]. For example, Sherbet et al. [31] used AI-based technology in cancer management, and Li et al. [37] proposed multi-resolution convolutional networks for lung nodule detection. However, the sMRI image, as an important assistance in AD diagnosis, is consisted of many brain scans, which contains more than millions of voxels, in contrast the number of existing samples is small. As a result, few works in AI for AD identification are proposed because of the small sample problem in the past. Additionally, features extracted from the sMRI image by AI-based technology are abstract, therefore it is difficult by means of those abstract features to find pathological tissues related to AD and give a reasonably biological explanation. But it can be believed that AI-based technology must be widely used for AD identification in the future with the number of AD samples increasing.

To make full use advantages of the spatial domain-based and the transformation domain-based methods, in this study, a novel method (namely AD-WTEF) is proposed to identify subjects with AD, MCI and HC by extracting the wavelet transformation energy feature (WTEF) from the sMRI image. After preprocessing for the sMRI image, we can get gray mater (GM), white mater (WM) and cerebrospinal fluid (CSF) tissue images of a brain. The GM image mostly related to AD is selected to be experimental data. To obtain the overall energy distribution of brain atrophies, each scan of the GM image is firstly transformed by wavelet in obtaining the directional subbands with the same size at different transformation levels. Secondly, based on anatomical automated labelling (AAL) atlas, a brain mask consisted of 90 regions of interest (ROIs) is constructed to segment the subbands at the same direction and transformation level into 90 energy ROIs (EROIs). And then, an energy feature is got by averaging coefficients in an EROI, following that an energy feature vector is formed to describe the subbands at the same direction and transformation level by connecting energy features of the 90 EROIs. These energy feature vectors are subsequently concatenated to be a WTEF for representing the sMRI image. Finally, the WTEF is input into the nearest neighbor (NN) classifier for AD identification. It is obvious that the sMRI image is firstly transformed by wavelet in the frequency domain, and then subbands are segmented to obtain the EROIs in the spatial domain. Therefore, advantages of the spatial domain-based and transformation domain-based methods are fully used by AD-WTEF, and associations between different brain tissue regions are implicitly maintained. Results of comparing with other seven state-of-the-art methods suggest that the AD-WTEF can effectively identify AD patients. Meanwhile, experiments to find ROI related to AD also indicate that our AD-WTEF can capture the subtle energy distribution differences reflected in the sMRI images of subjects with AD, MCI, and HC.

There are three main contributions in the AD-WTEF: (1) A framework using wavelet to transform the sMRI image into directional and multiscale subbands and then segmenting those subbands by a constructed brain mask is proposed to extract energy features for AD identification; (2) Instead of using AAL atlas directly to the GM image, the constructed brain mask that consists of 90 ROIs is used for reasonably segmenting these subbands into 90 EROIs; (3) The technique of multiscale analysis is introduced to transform scans of the sMRI image and construct energy feature vectors at different transformation levels in identifying AD patients, which provide new clues for understanding the pathology and new avenues to identify the brain diseases.

The rest of this paper is organized as follows. Section 2 gives some related works on AD identification. In Section 3, materials and methodology are introduced. Evaluation metrics and experimental results are included in Section 4. Discussion is shown in Section 5. Finally, conclusions are given in Section 6.

2. Related work

For the spatial domain-based method, much higher dimensionality of the voxel-based feature is usually noisy and most of the voxel-based features might be not related to AD [38–44]. Therefore features of considering regions of interest (ROI) of the brain tissue are proposed to depict the sMRI image [45–48]. Ahmed et al. [49] combined hippocampus visual features and cerebrospinal fluid (CSF) volume to yield an automatic classification framework for AD identification. Khedher et al. [50] presented a new computer aided diagnosis system that allows the early AD diagnosis by using tissue-segmented brain images. Although the dimensionality and noise of the ROI-based feature is reduced to some extent, only a part of the brain volume is used as features such as gray matter probability and hippocampal volumes [51–54]. It is hard to give a reliable representation of the sMRI image with multiple lesions occurred. For the usage of whole brain structural information, the brain surface-based features are constructed for AD identification by analyzing the cortical thickness or cortical curvature [55–57]. For example, Dai et al. [58] established a network based on a kernel-based method for each subject by using mean cortical thickness and the network edges for AD identification. The challenge of this kind of features is how to select vertexes of the brain cortex, and they also face the problem of higher dimensionality.

In the perspective of transformation, multi-scale analysis can be introduced to capture energy features of the sMRI image at different directions and decomposition levels. To the best of our knowledge, most of the features used to identify AD patients belong to the spatial domain-based. There were few existing features in accordance with the transformation domain-based method for AD identification in the past decade. In nowadays, the transformation domain-based method gradually appears, for example, Zhang et al. [59] utilized stationary wavelet entropy to extract the texture features of an MRI for AD classification. Jha et al. [60] proposed a novel computer-aided diagnosis (CAD) cascade model to discriminate patients with the AD from healthy controls by using the dual-tree complex wavelet transforms. In addition, Bendib et al. [61] introduced a new brain MRI segmentation framework that combines a powerful multiresolution/multiscale image analysis technique with a robust weakly used ensemble learning paradigm for the segmentation of gray matter, white matter, and cerebrospinal fluid. So, it is reasonable to introduce multi-resolution analysis to extract features from the sMRI image for AD identification.

In addition, Rafiee et al. [62] proposed a two-stage unsupervised segmentation approach based on ensemble clustering to extract the focused regions (namely, ROI) from low depth-of-field images. The first stage is to cluster image blocks in a joint contrast-energy feature space into three constituent groups. In stage two, a binary saliency map is constructed from the relevant blocks at the pixel level. Then a set of morphological operations is employed to create the ROI from the map. In Rafiee's segmentation approach, image blocks are represented by

features computed in spatial and frequency domains, which is similar with our proposed method in constructing features of the sMRI image. Obviously, Rafiee's segmentation approach is suitable to the low depth-of-field image, which is different from our proposed method used for the sMRI image. The reason is that the constructed brain mask based on AAL is not used to divide the sMRI image to obtain brain ROIs, but to divide the wavelet subbands to obtain subband EROIs; Furthermore, the sMRI is not a low depth-of-field image, but an image consisted of many scans, and ROIs of the AAL are defined by the experienced brain imaging specialist, which can ensure that features extracted from EROIs have specific biological meanings.

3. Materials and methodology

In this section, materials used in this study and their preprocessing are firstly introduced, and then methodology of extracting the wavelet transformation energy feature (WTEF) is given.

3.1. Materials

Data used in the preparation of this article were obtained from the Alzheimer's Disease Neuroimaging Initiative (ADNI) database (adni.loni.usc.edu). The ADNI was launched in 2003 as a public-private partnership, led by Principal Investigator Michael W. Weiner, MD. The primary goal of ADNI has been to test whether serial magnetic resonance imaging (MRI), positron emission tomography (PET), other biological markers, and clinical and neuropsychological assessment can be combined to measure the progression of mild cognitive impairment (MCI) and early Alzheimer's disease (AD).

In order to assess the performance of our AD-WTEF, we select 480 subjects from the ADNI database, composing of 90 AD, 280 MCI, and 110 HC subjects. Among the 280 MCI subjects, 120 subjects converted to AD after 18 months are denoted as MCIc, on the contrary, 160 subjects not converted to AD after 18 months are denoted as MCInc. The detail demographic information of all the 480 subjects is given in Table 1. MMSE, F, and M in Table 1 are abbreviations of Mini Mental State Examination, Female, and Male, respectively.

All selected subjects are preprocessed before they are used to test the AD-WTEF. Statistical parametric mapping (SPM8) [63] and voxel-based morphometry (VBM8) [6] software tools are selected to preprocess the sMRI images. After preprocessing steps of head motion correction, skull strap, segmentation, and smoothing, the size of a sMRI image is converted to $121 \times 145 \times 121$ gray matter (GM), cerebrospinal fluid (CSF), and white matter (WM) tissue images, and the voxel volume is $1.5 \times 1.5 \times 1.5\,\mathrm{mm}^3$. For a visual comparison of the original and the preprocessed MRI images, an example of four scans of a sMRI image is shown in Fig. 1.

At the experimental stage, the GM image mostly related to AD is selected to extract the WTEF, and four data sets are constructed to perform experiments, which are described as follows:

1. AD/HC: containing 90 AD and 110 HC subjects;
2. AD/MCI: containing 90 AD and 280 MCI subjects;
3. MCI/HC: containing 280 MCI and 110 HC subjects;
4. MCIc/MCInc: containing 120 MCIc and 160 MCInc subjects.

Table 1
Detail demographic information of the 480 subjects from the ADNI database.

Type	Gender (F/M)	Number	Age (mean ± deviation)	MMSE (mean ± deviation)
AD	40/50	90	76.93 ± 6.87	23.70 ± 3.55
MCIc	67/53	120	77.57 ± 9.81	26.66 ± 2.84
MCInc	71/89	160	74.73 ± 6.66	26.10 ± 3.88
MCI	138/142	280	75.95 ± 8.29	26.21 ± 3.78
HC	50/60	110	76.08 ± 4.98	28.24 ± 2.21

It can be seen that the MCIc/MCInc is a challenging data set, as subjects in this data set belong to the same stage of AD, and there are subtle differences between GM images of these subjects.

3.2. Methodology

After preprocessing to the sMRI images, we can get their GM images. Firstly, we use wavelet to transform scans of the GM image so that the constructed mask can be conveniently used to segment subbands of the scans at the same direction and transformation level in constructing energy features and energy feature vectors. The WTEF of a GM image can be then obtained by concatenating these energy feature vectors at different directions and transformation levels. Finally, the NN classifier is selected to identify subjects with AD, MCI and HC. Fig. 2 gives the flowchart of our AD-WTEF. In the following, we will introduce the process of extracting WTEF from the GM image.

According to previous works about AD identification, the GM image is divided into 90 (or 116, including 26 cerebellum tissue regions) regions of interest (ROIs) by a mask called anatomical automated labeling (AAL) atlas [64]. These ROIs are used to construct spatial structural features. Different from those existing methods, AD-WTEF transforms each scan of the GM image to obtain its directional and multiscale subbands. For simplicity, these GM images are represented by a subject set, $\{I_{(i,j)}\},\ i = 1,2,\ldots,N,\ j = 1,2,\ldots,M$, where $N = 480$ is the number of all subjects and $M = 121$ is the number of scans of a GM image.

Daubechies (db) wavelet has scaling and wavelet two functions. In multi-resolution analysis, the scaling function can be expressed as

$$\phi(x,y) = \sum_{k1=0}^{N1-1}\sum_{k2=0}^{N2-1} \alpha_{(k1,k2)}\phi(2x-k1, 2y-k2), \tag{1}$$

where $\alpha_{(0,0)},\ldots,\alpha_{(N1-1,N2-1)}$ are scaling coefficients. The wavelet function can be represented by a linear combination of the scaling functions

$$\psi(x,y) = \sum_{k1=0}^{M1-1}\sum_{k2=0}^{M2-1} \beta_{(k1,k2)}\phi(2x-k1, 2y-k2), \tag{2}$$

where $\beta_{(0,0)},\ldots,\beta_{(M1-1,M2-1)}$ are wavelet coefficients.

Given the jth scan of the ith GM image $I(i,j)$, we use db8 filter and stationary wavelet transformation-2 (swt2) to transform the scan into subbands with the same size at different transformation levels. After wavelet transformation, subbands of all scans are represented by $\{S^i_{j,l,k}\},\ l = 1,\ldots,L,\ k = 1,2,3,4$, where l is the lth transformation level and k is the kth directional subband of the scan at the lth level. Because of that each transformation can generate 4 direction subbands at each level, so the total number of subbands of the ith GM image by L times transformations is $4 \times M \times L$. For example, when $i = 1, j = 1, L = 1$, we can obtain 4 subbands of the 1th scan of the 1th GM image by $L = 1$ level transformation. Fig. 3 gives an instance of the wavelet transform on a scan with $L = 2$. There are 8 subbands in total with each of 4 subands at one level.

To capture the brain atrophy information spatially distributed in different energy regions of interest (EROIs), a brain mask is needed to be constructed based on AAL atlas [64]. The single ROI mask set is firstly made by using AAL atlas contained 90 ROIs without cerebellum, which is denoted as $\{\mathrm{AAL}_{p,t}\},\ p = 1,2,\ldots,90,\ t = 1,2,\ldots,91$, where p is the pth single ROI mask and t is the tth scan of the pth single ROI mask. While, size and voxel volume of the single ROI mask separately are $91 \times 109 \times 91$ and $2 \times 2 \times 2\,\mathrm{mm}^3$, which are not accordance with the size and the voxel volume of the preprocessed GM images. So co-registration needs to be done between the single ROI mask and the GM image by SPM8. After co-registration, size and voxel volume of the single ROI mask change as $121 \times 145 \times 121$ and $1.5 \times 1.5 \times 1.5\,\mathrm{mm}^3$, respectively. Therefore, the whole brain ROI mask, denoted as $\{\mathrm{Mask}_t\}$, can be constructed by the

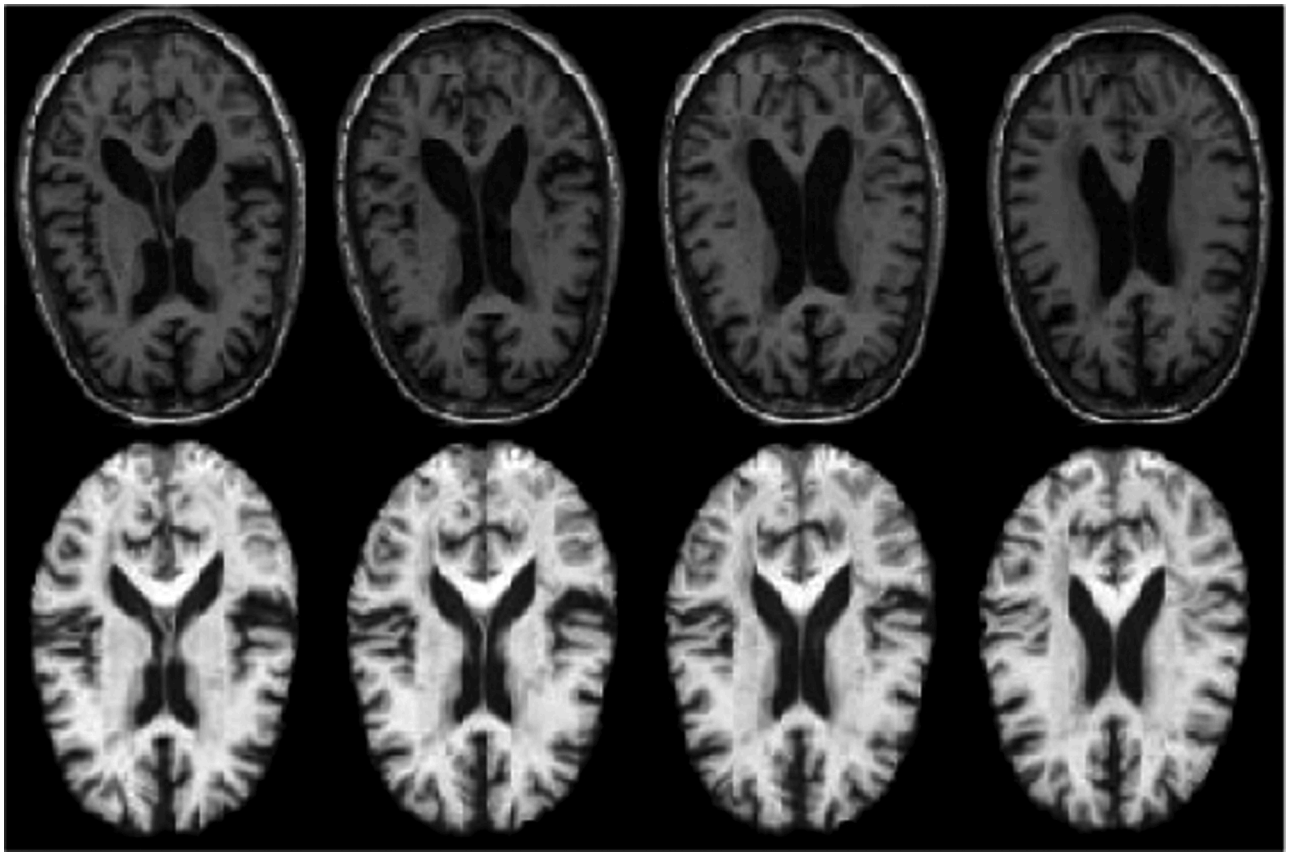

Fig. 1. An example of the original and the preprocessed sMRI images. The first row is original scans of the sMRI image; The second row is their corresponding preprocessed scans.

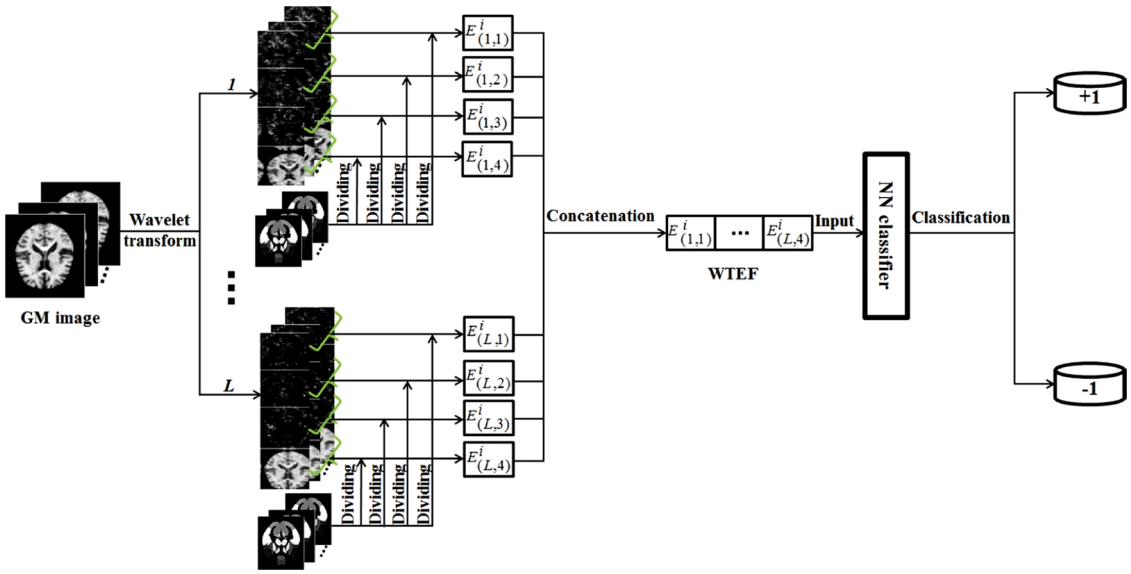

Fig. 2. The flowchart of our AD-WTEF in extracting the WTEF and performing AD identification using the NN classifier.

following equation:

$$\mathrm{Mask}_t(x,y) = p, \text{if} \mathrm{AAL}_{p,t}(x,y) = 1, p = 1,\ldots,90, \tag{3}$$

where (x,y) is a position in the pth brain tissue ROI of the tth scan, $t = 1, 2,\ldots,121$, $x \in [1,121]$, and $y \in [1,145]$. Fig. 4 shows six scans of the final constructed whole brain ROI mask.

Up to now, we have gotten subbands of GM images $\{S^i_{j,l,k}\}$ and a constructed mask $\{\mathrm{Mask}_t\}$. For subbands of the kth direction at the lth level of the ith GM image, an EROI set, $\{\mathrm{EROI}^i_{l,k,p}\}$, is represented by the following equation:

$$\mathrm{EROI}^i_{l,k,p} = \mathrm{EROI}^i_{l,k,p} \bigcup R_p(x,y), \quad p = 1,2,\ldots,90 \tag{4}$$

where

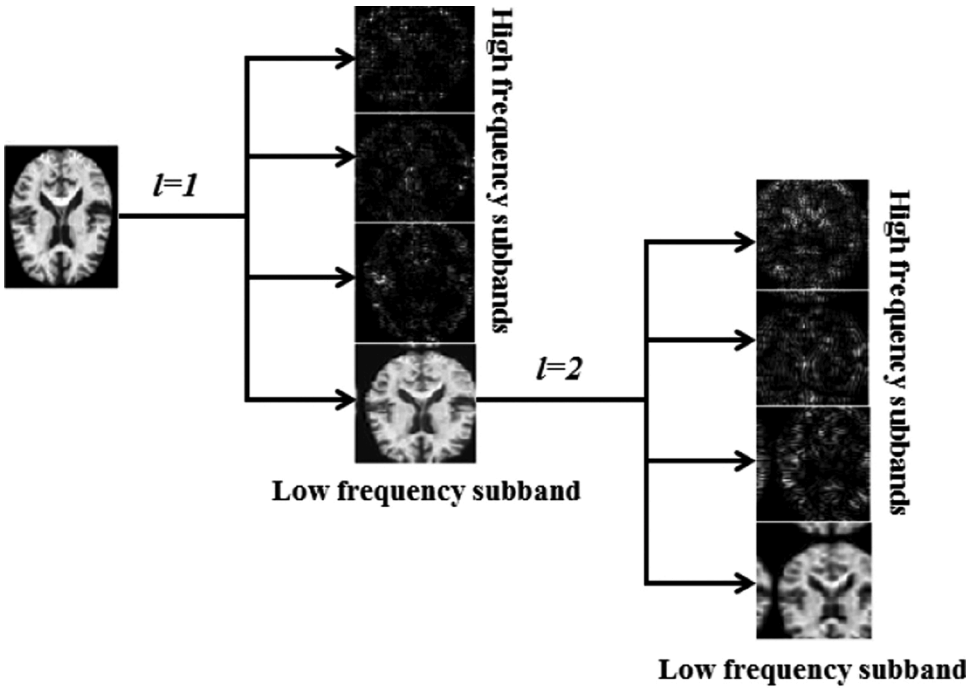

Fig. 3. An instance of the wavelet transform on a scan with $L = 2$.

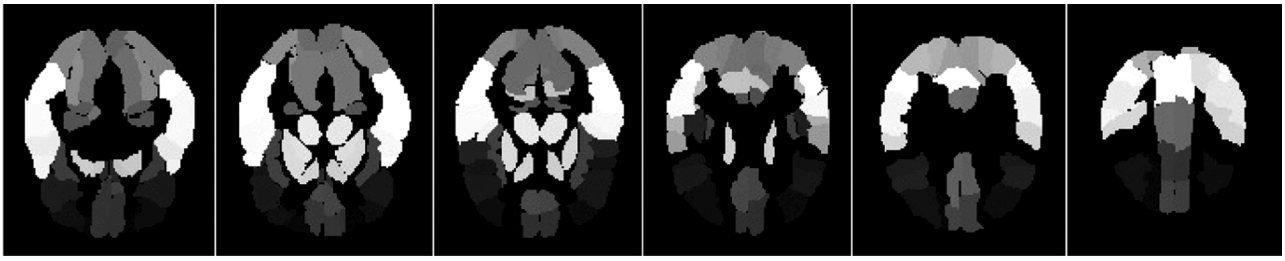

Fig. 4. Six scans of the constructed $Mask_t$ with their serial number $t = 32, 48, 54, 68, 71, 80$.

$$R_p(x,y) = \begin{cases} S^i_{.,l,k}(x,y), & \text{Mask}(x,y) = p \\ 0, & \text{Others} \end{cases} \tag{5}$$

The energy feature of an EROI of the kth direction at the lth level of the ith GM image can be computed by the following equation:

$$e^i_{(l,k,p)} = \frac{\sum_{m=1}^{M^i_{l,k,p}} \text{EROI}^i_{l,k,p}(m)}{M^i_{l,k,p}}, \quad p = 1, 2, \ldots, 90 \tag{6}$$

where $M^i_{l,k,p}$ is the total number of coefficients contained in the pth EROI of the kth direction at the lth level of the ith GM image. For the subbands at the same direction and transformation level, we can obtain an energy feature vector based on Eq. (6), which can be represented by the following equation:

$$E^i_{(l,k)} = [e^i_{(l,k,1)}, e^i_{(l,k,2)}, \ldots, e^i_{(l,k,90)}]. \tag{7}$$

Thus, the wavelet transformation energy feature (WTEF) of the ith subject is extracted from its GM image based on a constructed mask by the L-level wavelet transform, which is denoted as following:

$$\text{WTEF}^i = [E^i_{(1,1)}, \ldots, E^i_{(1,4)}, \ldots, E^i_{(L,1)}, \ldots, E^i_{(L,4)}]. \tag{8}$$

For simplicity, the extracted WTEFs of all GM images of the subjects selected from ADNI database are denoted as a feature set, $\{\text{WTEF}^i\}$, $i = 1, 2, \ldots, N$.

Finally, the nearest neighbor (NN) classifier with chi-square distance is selected to classify those testing subjects in the experimental stage. Giving two extracted WTEFs denoted as V_1 and V_2, the chi-square distance $D(V_1, V_2)$ between them is calculated by

$$D(V_1, V_2) = \sum_{n=1}^{Q} \frac{(V_1(n) - V_2(n))^2}{V_1(n) + V_2(n)}, \tag{9}$$

where Q is the total number of all feature elements in each vector of V_1 and V_2. In the classification phase, an unlabeled subject will be categorized into the class whose chi-square distance D is minimum.

4. Evaluation metrics and experimental results

In this section, Evaluation metrics used in this study are firstly introduced. Subsequently, we give results of comparing with other seven state-of-the-art methods. Finally, we estimate the optimal value of the wavelet transform level L by experiments on the four data sets.

4.1. Evaluation metrics

With obtained optimal estimation parameter $L = 1$, we will conduct experiments on AD/HC, AD/MCI, MCIc/MCInc and MCI/HC four data sets. At the experimental stage, we will perform $n = 10$ experiments with ten-fold cross validation on each of these four data sets. We use average classification accuracy (ACC), average specificity (Sp) and

average sensitivity (Se) of the ten experiments on each of the four data sets as evaluation metrics, which are expressed by formulas as

$$\mathrm{ACC} = \frac{1}{n}\sum_{i=1}^{n}\frac{\mathrm{TP}_i + \mathrm{TN}_i}{\mathrm{TP}_i + \mathrm{FP}_i + \mathrm{TN}_i + \mathrm{FN}_i}, \tag{10}$$

$$\mathrm{Sp} = \frac{1}{n}\sum_{i=1}^{n}\frac{\mathrm{TN}_i}{\mathrm{FP}_i + \mathrm{TN}_i}, \tag{11}$$

$$\mathrm{Se} = \frac{1}{n}\sum_{i=1}^{n}\frac{\mathrm{TP}_i}{\mathrm{TP}_i + \mathrm{FN}_i}, \tag{12}$$

where TP_i is the number of correctly classified true positive subjects in the ith experiment, FP_i is the number of incorrectly classified negative subjects in the ith experiment, TN_i is the number of correctly classified true negative subjects in the ith experiment, and FN_i is the number of incorrectly classified positive subjects in the ith experiment.

4.2. Experimental results

In this part, we compare our AD-WTEF with seven state-of-the-art methods. Jha et al. [59] extracted feature using the dual-tree complex wavelet transforms. Ahamed et al. [49] combined hippocampus visual features and cerebrospinal fluid (CSF) volume to yield an automatic classification framework. Zhang et al. [60] utilized stationary wavelet entropy to extract the texture features of an MRI. Khedher et al. [50] presented a new computer aided diagnosis system using tissue-segmented brain images. Dai et al. [58] established a network based on a kernel-based method for each subject by using mean cortical thickness and the network edges. For the method proposed by Li et al. [8], it is a method of segmenting hippocampus from the MRI image by deep learning, and we can directly use the hippocampus as feature of the sMRI image in AD identification. Ju et al. [52] constructed a brain network by computing the functional connectivity of brain regions.

In the diagnosis of Alzheimer's disease (AD), identifying AD patients from health control (HC) subjects is a very primary work, which will have a large impact on a patient in clinic. Hence, the first comparison experiment is conducted on the AD/HC data set. Results of the other seven state-of-the-art comparison approaches and the proposed AD-WTEF are listed in Table 2. According to Table 2, it can be seen that ACC of the proposed AD-WTEF outperforms the results of the other seven comparative methods, which reaches to 93.93%. Obviously this result of our AD-WTEF is better than 92.91% of the best comparative method, and has 1.02% improvements, which means that there are more rooms for the AD-WTEF to improve its classification performance. In addition, Se and Sp of the proposed AD-WTEF are also better than those of the best comparative method, and the gaps are 1.17% and 0.47%, respectively. Experimental results shown in Table 2 demonstrate the reasonableness of using the wavelet transform technique for the sMRI image.

Once a person is diagnosed as a patient with AD, identification of the stage is very important. So experiments on MCI/HC and AD/MCI data sets are also performed to compare with the other seven comparative methods. And experimental results are shown in Tables 3 and 4 , respectively. From experimental results of Tables 3 and 4, it can be seen that performance of the proposed AD-WTEF is slightly inferior to the best comparative method on MCI/HC data set, and marginally superior to the best comparative method on AD/MCI data set. There are two-fold reasons to this phenomenon, firstly, MCI is an asymptomatic and transitional stage of AD, the conversion of a health person from health control stage to mild cognitive impairment stage produces subtle structural and functional changes in MRI images of the brain. Therefore, these changes are very difficult to be captured not only by energy features extracted based on the wavelet transform, but also by the other spatial features. Secondly, the wavelet transform is a process with information redundancy, some useful and discriminative information is possibly covered up by redundancy, eventually causing the discriminative performance decrease of the proposed AD-WTEF. Explanations to this phenomenon also indicate the research direction of reducing redundancy of the wavelet transform and capturing fine information of the sMRI image in our future work.

Prediction of conversion from MCI to AD is of crucial importance, for that, it is very necessary to classify mild cognitive impairment (MCI) subjects into MCIc who will convert to AD after 18 months and MCInc who will not convert into AD after 18 months. To validate this ability of the proposed AD-WTEF, MCIc/MCInc data set is constructed to test the proposed AD-WTEF, and ACCs of the other seven comparison approaches and the proposed AD-WTEF are shown in Table 5. It can be seen from Table 5 that ACC, Se and Sp of the proposed AD-WTEF consistently outperform those of the best comparative method, which have 1.62%, 0.37%, and 1.08% improvements respectively. Experimental results on the challenging MCIc/MCInc data set further demonstrate the effectiveness of the proposed AD-WTEF in prediction of a person with converted MCI from stable MCI patient.

To extensively verify the discrimination of the proposed AD-WTEF, we compare WTEF with voxel, volume, and cortical thickness-based features on AD/HC, AD/MCI, MCI/HC, and MCIc/MCInc data sets using nearest neighbor (NN) classifier. For the NN classifier, we use the Chi-square distance shown in Eq. (9) as its metric. In the following, the voxel-based feature extracted by making statistics on voxels is denoted as VoxF, the volume-based feature extracted by summing voxels in the volume that is segmented from the GM image is denoted as VolF, and the cortical thickness-based feature extracted by computing distances of the cortical thickness is denoted as CorTF. ACCs of VoxF+NN, VolF+NN, CorTF+NN, and the proposed WTEF+NN are listed in Table 6. It is obviously seen from Table 6 that the proposed WTEF consistently outperforms the VoxF, VolF, and CorTF in terms of using the NN classifier, which demonstrate the discriminative performance of the proposed WTEF. The reason is three-fold: Firstly, the GM image is analyzed globally, which can guarantee that more useful information is extracted and contained in the energy features; Secondly, wavelet transformation can effectively capture direction and multiscale information of the GM image, which can relatively be better to represent subtle differences between GM images of subjects with AD, MCI and HC; Thirdly, advantages both of the spatial and the transformation domain-based methods are contained in the proposed AD-WTEF, so, the proposed WTEF can

Table 2
Experimental ACCs, Ses, and Sps of the other seven state-of-the-art comparison approaches and the AD-WTEF on AD/HC data set.

Method	ACC (%)	Se (%)	Sp (%)
Jha et al. [59]	90.16	90.22	90.15
Ahmed et al. [49]	86.40	77.61	93.28
Zhang et al. [60]	92.70	92.67	92.77
Khedher et al. [50]	88.96	92.35	86.24
Dai et al. [58]	90.81	92.59	90.33
Li et al. [8]	87.51	87.60	87.42
Ju et al. [52]	92.91	93.00	92.85
AD-WTEF	93.93	94.17	93.75

Table 3
Experimental ACCs, Ses, and Sps of the other seven state-of-the-art comparison approaches and the AD-WTEF on MCI/HC data set.

Method	ACC (%)	Se (%)	Sp (%)
Jha et al. [59]	81.94	75.79	84.18
Ahmed et al. [49]	76.29	72.30	81.53
Zhang et al. [60]	80.67	76.79	86.98
Khedher et al. [50]	82.41	84.12	80.48
Dai et al. [58]	81.92	78.51	80.34
Li et al. [8]	79.35	79.44	79.26
Ju et al. [52]	81.17	82.26	81.11
AD-WTEF	82.12	78.29	87.00

Table 4
Experimental ACCs, Ses, and Sps of the other seven state-of-the-art comparison approaches and the AD-WTEF on AD/MCI data set.

Method	ACC (%)	Se (%)	Sp (%)
Jha et al. [59]	78.48	75.35	79.98
Ahmed et al. [49]	74.51	77.94	71.23
Zhang et al. [46]	85.89	72.21	88.65
Khedher et al. [50]	84.53	88.75	83.07
Dai et al. [58]	85.92	82.46	87.59
Li et al. [8]	77.25	77.34	77.16
Ju et al. [52]	84.37	85.46	84.31
AD-WTEF	86.40	82.11	89.91

Table 5
Experimental ACCs, Ses, and Sps of the other seven state-of-the-art comparison approaches and the proposed AD-WTEF on MCIc/MCInc data set.

Method	ACC (%)	Se (%)	Sp (%)
Jha et al. [59]	69.21	70.74	67.45
Ahmed et al. [49]	68.72	67.38	70.69
Zhang et al. [60]	72.86	69.55	75.49
Khedher et al. [50]	70.11	68.61	74.16
Dai et al. [58]	71.04	65.98	75.56
Li et al. [8]	69.38	69.47	69.29
Ju et al. [52]	72.32	70.41	75.26
AD-WTEF	74.48	71.11	76.64

Table 6
ACCs (%) of VoxF+NN, VolF+NN, CorTF+NN, and the WTEF+NN on AD/HC, AD/MCI, MCI/HC and MCIc/MCInc data sets.

Features	AD/HC	AD/MCI	MCI/HC	MCIc/MCInc
VoxF+NN	80.71	60.87	78.80	55.00
VolF+NN	67.75	63.68	63.39	56.91
CorTF+NN	89.71	69.04	62.52	59.05
WTEF+NN	93.93	86.40	82.12	74.48

properly describe the sMRI image.

Experimental results indicate that wavelet can be used to analyze the sMRI image in the frequency domain. Even though, sMRI is a kind of image containing a lot of noise and redundant information, which can be suppressed by the wavelet transformation. Therefore, energy distributions of the sMRI image can be depicted by directional and multiscale subbands. Additionally, we use the constructed brain mask to segment those wavelet subbands for obtaining EROIs, which guarantee that the energy distribution can be properly captured by the proposed WTEF. Finally, comparisons with the state-of-the-art methods on the four data sets testify that the AD-WTEF has the satisfactory discrimination and efficient performance in identifying subjects among AD, MCI and HC.

Finally, we also give the mean running time (MRT, in seconds) of seven comparative methods and our AD-WTEF approach on MCIc/MCInc data set in identifying 140 subjects. The programs all run on Matlab R2017a and computer with Intel(R) Core(TM) i7-4700 3.40GHz CPU 64bit system. MRTs of Jha et al. [59], Ahamed et al. [49], Zhang et al. [60], Khedher et al. [50], Dai et al. [58], Li et al. [8], Ju et al. [52], and our AD-WTEF are 7.37 s, 2.17 s, 8.46 s, 4.15 s, 10.03 s, 50.18 s, 83.01 s, and 5.41 s respectively. Obviously, MRT of our AD-WTEF is superior to those of wavelet based [59,60], cortical network based [58] and deep learning based [8,52] methods, but is inferior to those of spatial domain-based method [49,50], which means our AD-WTEF is relatively efficient in AD identification. In AD-WTEF, wavelet transformation is time-consuming, taking more than half the MRT.

4.3. Parameter estimation

Obviously, in the proposed method, parameters of the wavelet transform level L and the number of nearest neighbors K in the K-NN classifier need to be estimated for achieving an optimal performance in the classification stage. For the purpose of getting optimal estimation values of the wavelet transform level L and the number of nearest neighbors K, we conduct multiple estimation experiments on those four data sets. In each of these estimation experiments, ten-fold cross validation are performed, and each experiment are done ten times to obtain an average classification accuracy (ACC) as the unbiased experimental result.

Fig. 5(a) shows ACCs of experiments on the four data sets with $L = 1, 2, 3$. According to Fig. 5(a), it can be seen that the proposed AD-WTEF can obtain a best ACC when $L = 1$. Meanwhile, with the increase of L, ACCs of the proposed AD-WTEF decrease drastically. There are threefold reasons for this phenomenon. Firstly, the wavelet transformation is different from the wavelet decomposition, which is a transformation with information redundancy, with the increase of L, more redundant information will be contained in the subbands, which is a main cause of decreasing the ACC. Secondly, the dimensionality of the proposed WTEF is related to L, hence, the number of energy features contained in the WTEF will be severely increased, and the stability of the structure of the proposed WTEF will become worse with L increasing. For example, when $L = 3, 4$, the dimensions of the WTEF are $90 \times 4 \times 3 = 1080$ and $90 \times 4 \times 4 = 1440$, respectably. Thirdly, with the increase of L, more macrostructural information is being predominant, nonetheless, the identification of AD from HC subjects mainly depends on microstructural differences, which is another cause of decreasing the ACC.

For the K-NN classifier, Fig. 5(b) shows ACCs of experiments on the four data sets with different K values. As shown clearly in Fig. 5(b) where ACCs gradually decrease with the increase of K and the proposed WTEF can get the best experimental results when $K = 1$. Hence, the NN (namely 1-NN) classifier is selected to categorize subjects with AD, MCI and HC in this study.

In summary, $L = 1$ is selected to be the optimal estimation value of wavelet transformation level, which implicitly reduces the dimensionality of the proposed WTEF to some extent. Meanwhile, the NN classifier is selected for AD classification. In terms of ACCs shown in Fig. 5, $L = 1$ and $K = 1$ are used as the optimal parameter estimation values.

5. Discussion

In this section, we will find brain ROIs (corresponding to EROIs segmented from subbands, in the following, we consistently use ROI) related to AD by testing the discrimination of energy features of the 90 ROIs. Due to the fact that each hemisphere of a brain contains 45 ROIs and the brain is symmetric, so ROIs in each hemisphere with the same name, for example precentral-gyrus-left and precentral-gyrus-right regions, are regarded as one region in the following experiments to find ROI related to AD. That is, there are 45 ROIs left to be confirmed. And the serial number of each ROI is listed in Table 7. Moreover we regard ACC of the AD-WTEF as a reference, which means that a ROI will make the negative contribution to AD identification when ACC of the AD-WTEF with the ROI removed outperforms the reference, and vice versa.

Firstly, we mainly find which ROI is discriminative in identifying AD from HC subjects. ACCs of the AD-WTEF with one ROI removed and the AD-WTEF on the AD/HC data set are shown in Fig. 6. As shown in Fig. 6, there are heterogeneous discriminative powers for different ROIs in diagnosing a subject whether with AD or not, which validates that Alzheimer is a disease that spans multiple ROIs and lesions of the ROIs are different. Additionally, from Fig. 6, it can be seen that the fist ten positive ROIs related to AD, numbered as 1 (precentral gyrus), 2 (superior frontal gyrus), 4 (middle frontal gyrus), 10 (supplementary motor area), 15 (Insula), 17 (median cingulate paracingulate gyri), 20 (parahippocampus), 21 (amygdala), 32 (supramarginal gyrus), and 40 (heschl gyrus) based on Table 7, have made more contributions definitely in identifying AD, which consist with the findings of existing works [65,66]. While compared with those previous works, we also find another some ROIs related to AD identification, such as 10 (supplementary

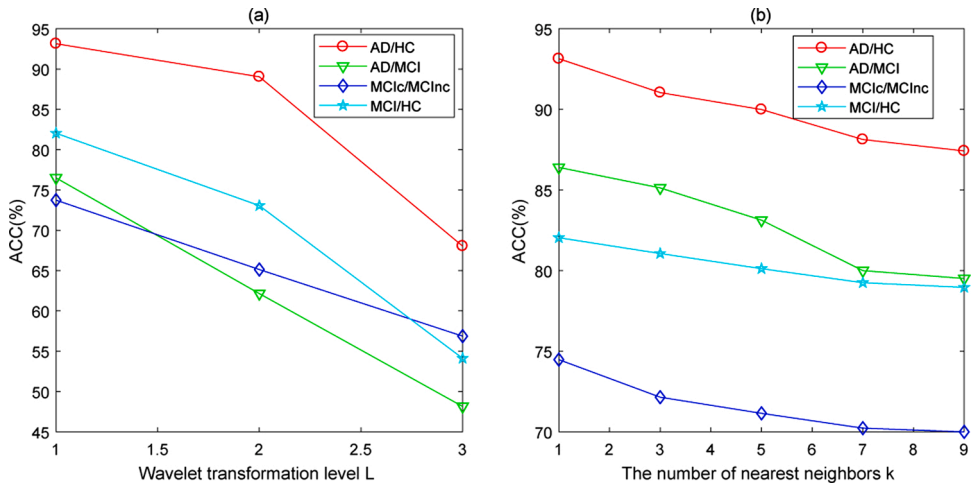

Fig. 5. Parameter estimation experiments on AD/HC, AD/MCI, MCIc/MCInc and MCI/HC four data sets. (a) ACCs of experiments on four data sets with $L = 1, 2, 3$. (b) ACCs of experiments on four data sets with different K values.

Table 7
Forty-five ROIs contained in a brain. Owing to the symmetry of a human brain, each ROI name corresponds to two brain regions. In fact, there are 90 ROIs in a brain.

Number	Brain ROI name	Number	Brain ROI name	Number	Brain ROI name
1	Precentral-Gyrus	16	Anterior-Cingulate-Paracingulate-Gyri	31	Inferior-Parietal-Gyri
2	Superior-Frontal-Gyrus	17	Median-Cingulate-Paracingulate-Gyri	32	Supramarginal-Gyrus
3	Superior-Frontal-Gyrus-Orbital	18	Posterior-Cingulate-Gyrus	33	Angular-Gyrus
4	Middle-Frontal-Gyrus	19	Hippocampus	34	Precuneus
5	Middle-Frontal-Gyrus-Orbital	20	Parahippocampus	35	Paracentral-Lobule
6	Inferior-Frontal-Gyrus-Opercular	21	Amygdala	36	Caudate-Nucleus
7	Inferior-Frontal-Gyrus-Triangular	22	Calcarine-Fissure-Surrounding-Cortex	37	Lenticular-Nucleus-Putamen
8	Inferior-Frontal-Gyrus-Orbital	23	Cuneus	38	Lenticular-Nucleus-Pallidum
9	Rolandic-Operculum	24	Lingual-Gyrus	39	Thalamus
10	Supplementary-Motor-Area	25	Superior-Occipital-Gyrus	40	Heschl-Gyrus
11	Olfactory-Cortex	26	Middle-Occipital-Gyrus	41	Superior-Temporal-Gyrus
12	Superior-Frontal-Medial	27	Inferior-Occipital-Gyrus	42	Temporal-Pole-Superior-Temporal
13	Superior-Frontal-Gyrus-Medial-Orbital	28	Fusiform-Gyrus	43	Middle-Temporal-Gyrus
14	Gyrus-Rectus	29	Postcentral-Gyrus	44	Temporal-Pole-Middle-Temporal
15	Insula	30	Superior-Parietal-Gyrus	45	Inferior-Temporal-Gyrus

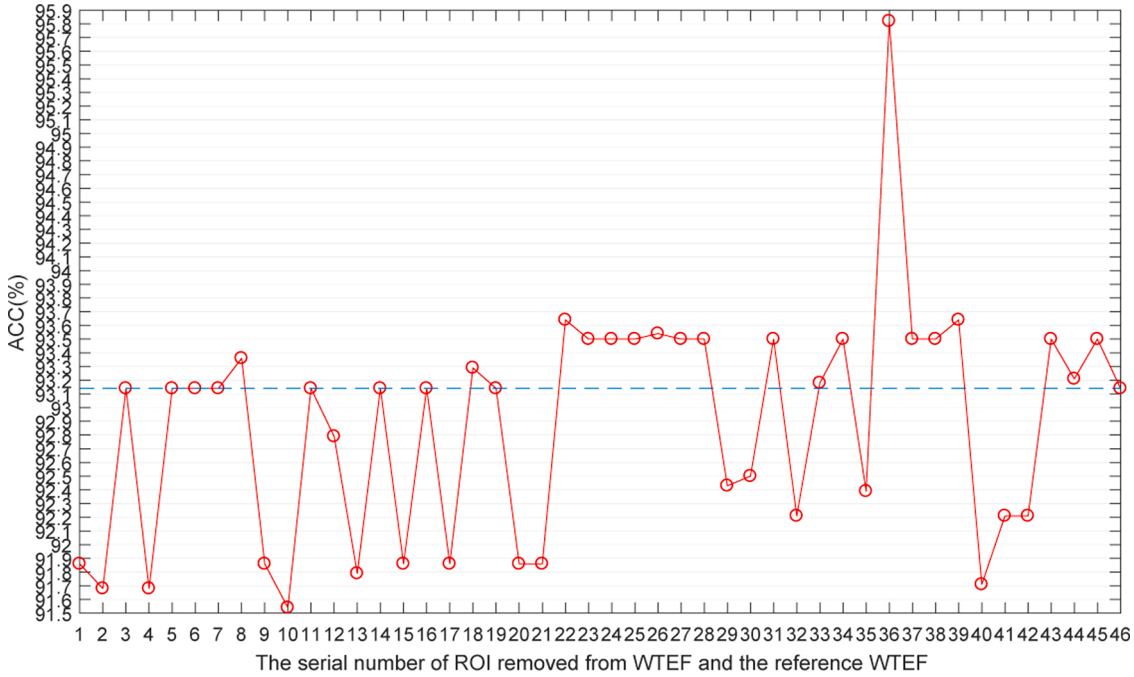

Fig. 6. ACCs of the AD-WTEF with one ROI removed on the AD/HC data set. Names of removed ROIs are listed in Table 7. The AD-WTEF is numbered as 46.

motor area) and 32 (supramarginal gyrus). However, some ROIs such as 22 (calcarine fissure surrounding cortex) and 26 (middle occipital gyrus), have made negative contributions to identifying AD. According to Fig. 6, ACC of the AD-WTEF is further improved when a negative ROI is excluded, and ACC of the AD-WTEF has reached to 95.85%.

To find important ROIs in identifying AD from MCI subjects, experiments with one ROI removed are also performed on the AD/MCI data set, and ACCs of the AD-WTEF with one ROI removed and the AD-WTEF are shown in Fig. 7. As shown in Fig. 7, all ROIs are categorised into positive contribution and negative contribution classes, no-contribution ROI is not found. Less than half of the ROIs do positive contributions in identifying AD from MCI subjects, the reason is that subjects with MCI are heterogeneous and MCIc patients have AD-like atrophy patterns in their MRI images. And ACC of the AD-WTEF has reached to 88.65% with a redundant ROI excluded in identifying AD from MCI subjects. In addition, the first ten positive ROIs numbered as 1 (precentral gyrus), 11 (olfactory cortex), 12 (superior frontal medial), 19 (hippocampus), 21 (amygdala), 22 (calcarine fissure surrounding cortex), 31 (inferior parietal gyri), 35 (paracentral lobule), 39 (thalamus), and 40 (heschl gyrus), are more discriminative in identifying AD from MCI subjects. However, there are relatively more negative ROIs, such as 18 (posterior cingulate gyrus), 20 (parahippocampus), and 36 (caudate nucleus). Results of this experiment show that differences between the sMRI images of subjects with AD and MCI can be captured by the WTEF, and also verify the reasonability of using the wavelet transform to the brain image and of treating the sMRI image as a whole in extracting the energy features.

To further obtain important ROIs related to AD in identifying MCI patients from HC subjects, experiments with one ROI removed are conducted on the MCI/HC data set, and Fig. 8 shows ACCs of the AD-WTEF with one ROI removed and the AD-WTEF. As shown in Fig. 8, most of ROIs do cooperative contributions to identifying MCI from HC subjects. While some ROIs such as 30 (superior parietal gyrus) deteriorate the discrimination of the AD-WTEF, and ACC of the AD-WTEF changes from 80.85% to 83.05% when only a negative ROI is removed, so feature selection in the final stage of extracting features from the sMRI image is absolutely necessary. According to Fig. 8, the first ten positive ROIs related to AD are 9 (rolandic operculum), 10 (supplementary motor area), 12 (superior frontal medial), 14 (gyrus rectus), 21 (amygdala), 32 (supramarginal gyrus), 34 (precuneus), 35 (paracentral lobule), 36 (caudate nucleus), and 40 (heschl gyrus). There are eight negative ROIs, including 6 (interior frontal gyrus opercular), 8 (interior frontal gyrus orbital), 22 (calcarine fissure frontal cortex) and so on. Additionally, 24 (lingual gyrus), 25 (superior occipital gyrus), 28 (fusiform gyrus), and 31 (interior parietal gyri) are no-contribution ROIs in identifying MCI from HC subjects.

To find the useful ROIs in differentiating MCIc from MCInc patients, experiments of the AD-WTEF with one ROI removed are performed on the MCIc/MCInc data set. ACCs of the AD-WTEF with one ROI removed and the AD-WTEF are shown in Fig. 9. From ACCs of Fig. 9, most of ROIs make a positive contribution to identifying MCIc from MCInc patients, but the contribution is small. Therefore, we can get the conclusion that lesions of different ROIs at MCI stage are subtle, but have occurred in many regions, and cognitive function of a person is gradually declining with the development of brain lesions. Hence, identifying MCIc from MCInc patients makes more sense and is important in clinic. As is shown in Fig. 9, the first ten positive ROIs related to AD are 1 (precentral gyrus), 2 (superior frontal gyrus), 9 (rolandic operculum), 10 (supplementary motor area), 12 (superior frontal medial), 19 (hippocampus), 20 (parahippocampus), 21 (amygdala), 35 (paracentral lobule), and 44 (temporal pole middle temporal), respectively. While only five ROIs are negative and two ROIs are no-contribution. Considering the findings of experiments on MCIc/MCInc data set, it validates again that the wavelet can be used to transform the sMRI image for extracting energy features from its subbands.

According to the experiments above, it can be found that ROIs such as 2 (superior frontal gyrus), 4 (middle frontal gyrus), 10 (supplementary motor area), 12 (superior frontal medial), 21 (amygdala), 35

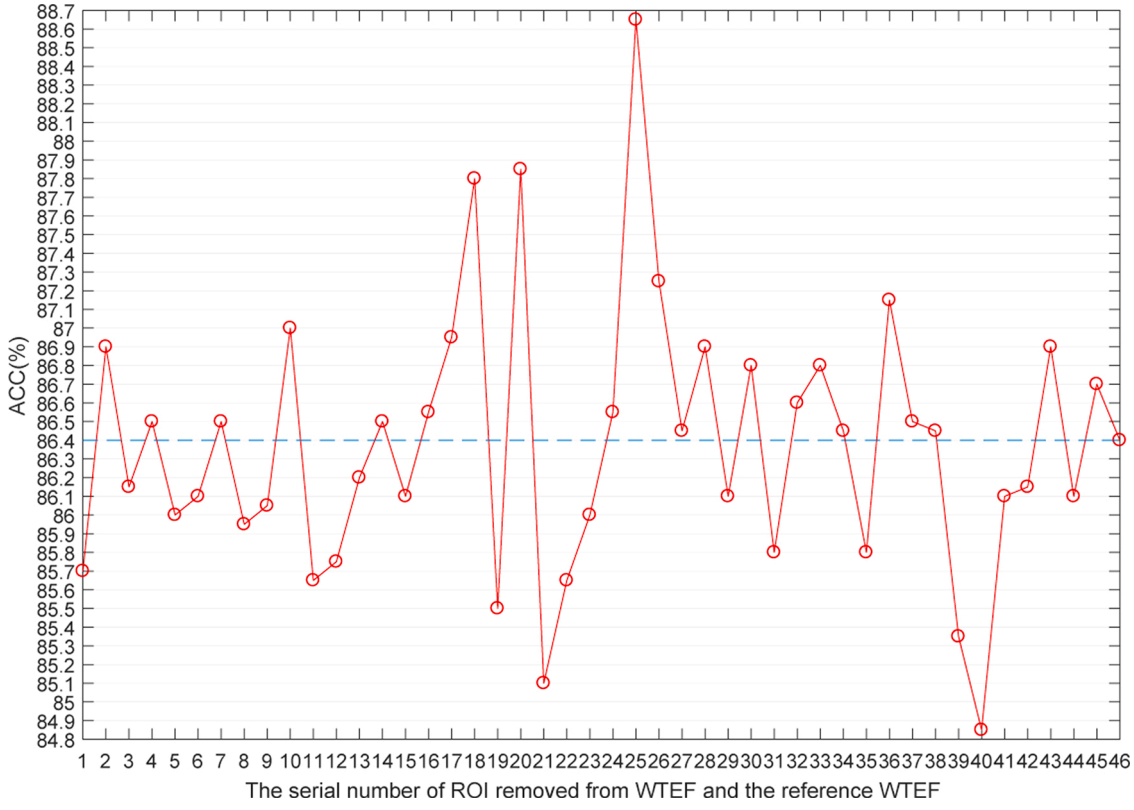

Fig. 7. ACCs of the AD-WTEF with one ROI removed on the AD/MCI data set. Names of removed ROIs are listed in Table 7. The AD-WTEF is numbered as 46.

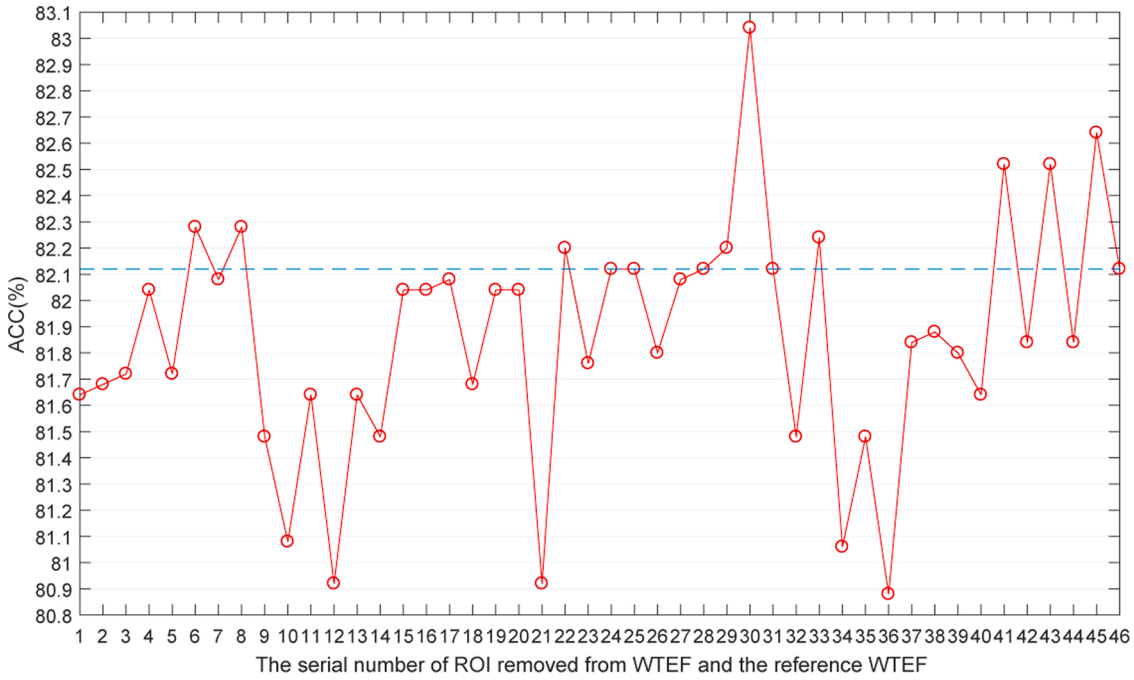

Fig. 8. ACCs of the AD-WTEF with one ROI removed on the MCI/HC data set. Names of removed ROIs are listed in Table 7. The AD-WTEF is numbered as 46.

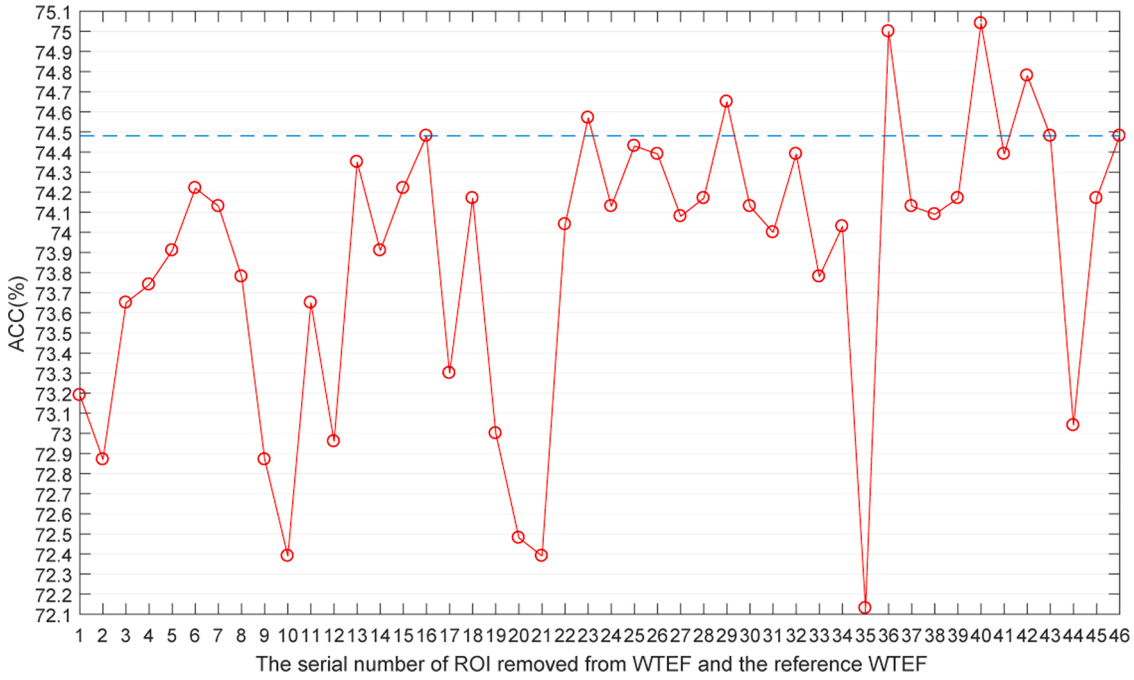

Fig. 9. ACCs of the AD-WTEF with one ROI removed on the MCIc/MCInc data set. Names of removed ROIs are listed in Table 7. The AD-WTEF is numbered as 46.

(paracentral lobule), and 36 (caudate nucleus), are important in diagnosing AD patients. For the four experiments to find ROI related to AD, we find that 21 (amygdala) is the only brain tissue that is consistently appeared in the fist ten ROIs, and differences of subtle tissue lesions can be captured by the AD-WTEF in differentiating subjects with AD, MCI, and HC. For the sake of visualization and clarity, the first ten positive ROIs found on the AD/HC, AD/MCI, MCI/HC and MCIc/MCInc data sets are separately depicted in Fig. 10, which are marked in red. It is clear from Fig. 10 that not all the brain tissues play the same important role in identifying AD. It implicitly means that the degree of brain lesions is different at different stages of AD. So feature selection is apparently needed so that those discriminative features can be extracted. Furthermore, it also verifies that the transformation domain-based tool can be used for analyzing the sMRI image. Overall, experiments to find ROI related to AD on four data set demonstrate the rationality of using wavelet to extract energy features from the sMRI image.

6. Conclusions

In this study, a novel method (namely AD-WTEF) is proposed to represent the sMRI image by extracting the wavelet transformation energy feature (WTEF) based on the constructed brain mask in

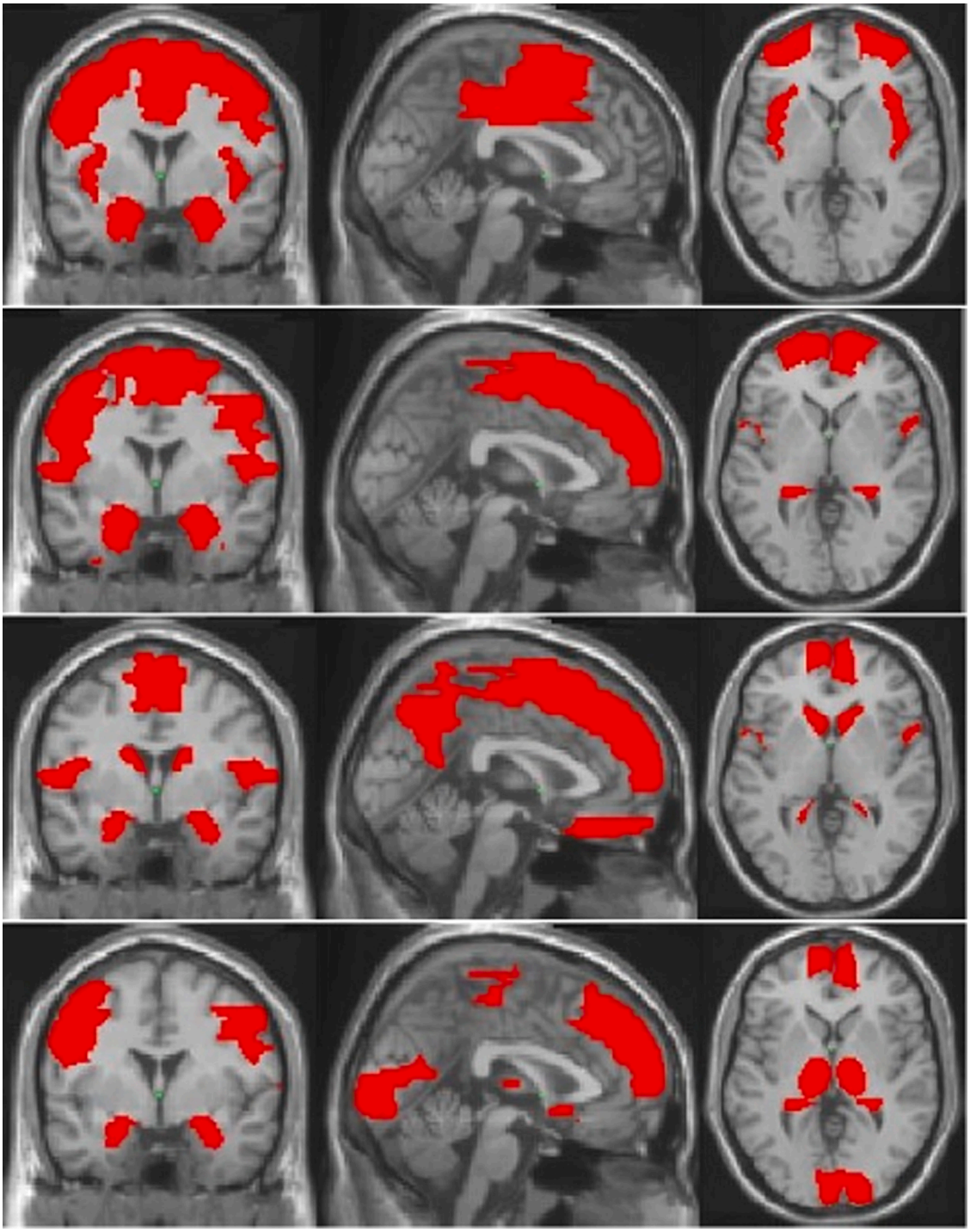

Fig. 10. First ten positive brain ROIs in identifying subjects with AD, MCI, and HC. The first row is on the AD/HC data set, the second row is on the MCIc/MCInc data set, the third row is on the MCI/HC data set, and the last row is on the AD/MCI data set. (For interpretation of the references to color in this figure legend, the reader is referred to the web version of this article.)

automatically identifying AD patients. Concretely, scans of the processed sMRI image are firstly transformed into directional and multi-scale subbands by wavelet. And then the subbands are segmented based on the constructed brain mask to obtain EROIs in constructing their subband energy feature vectors. By concatenating those energy feature vectors, we can obtain WTEF of the sMRI image. Experimental results demonstrate that AD-WTEF can effectively identify AD patients, owing to the fact that advantages both of the spatial domain-based and the transformation domain-based methods are fully used and subbands can be reasonably segmented by the constructed brain mask. However, there are some drawbacks of the proposed AD-WTEF, for example, the wavelet transform is a non-downsampling process which causes information redundancy, and the negative ROIs are also used to construct the WTEF. Thus, the contourlet transform is suggested to be used for reducing the information redundancy, and appropriate brain region selections are also suggested to find those ROIs related to AD when extracting energy features. Therefore, in our future work, we will focus on reducing the information redundancy. In addition, exploring network information or dynamical information to improve the accuracy (e.g. fMRI data) by network biomarker [67] or dynamic network biomarker [68] is also an

important future topic in identification of AD from HC subjects.

Conflict of interest

The authors declare no conflict of interest.

Acknowledgements

This paper was supported by the National Natural Science Foundation of China (Grant No. 61873202, 31930022, 61473232, 91430111, 31771476, 81471047, and 11871456), National Key R&D Program (Grant No. 2017YFA0505500 and 2016YFC0903400), Strategic Priority Research Program of the Chinese Academy of Sciences (Grant No. XDB38040400), Natural Science Foundation of Shanghai (Grant No. 17ZR1446100), and Shanghai Municipal Science and Technology Major Project (Grant No. 2017SHZDZX01).

Data collection and sharing for this project was funded by the Alzheimer's Disease Neuroimaging Initiative (ADNI) (National Institutes of Health Grant U01 AG024904) and DOD ADNI (Department of Defense award number W81XWH-12-2-0012). ADNI is funded by the National Institute on Aging, the National Institute of Biomedical Imaging and Bioengineering, and through generous contributions from the following: AbbVie, Alzheimer's Association; Alzheimer's Drug Discovery Foundation; Araclon Biotech; BioClinica, Inc.; Biogen; Bristol-Myers Squibb Company; CereSpir, Inc.; Cogstate; Eisai Inc.; Elan Pharmaceuticals, Inc.; Eli Lilly and Company; EuroImmun; F. Hoffmann-La Roche Ltd and its affiliated company Genentech, Inc.; Fujirebio; GE Healthcare; IXICO Ltd.; Janssen Alzheimer Immunotherapy Research & Development, LLC.; Johnson & Johnson Pharmaceutical Research & Development LLC.; Lumosity; Lundbeck; Merck & Co., Inc.; Meso Scale Diagnostics, LLC.; NeuroRx Research; Neurotrack Technologies; Novartis Pharmaceuticals Corporation; Pfizer Inc.; Piramal Imaging; Servier; Takeda Pharmaceutical Company; and Transition Therapeutics. The Canadian Institutes of Health Research is providing funds to support ADNI clinical sites in Canada. Private sector contributions are facilitated by the Foundation for the National Institutes of Health (www.fnih.org). The grantee organization is the Northern California Institute for Research and Education, and the study is coordinated by the Alzheimer's Therapeutic Research Institute at the University of Southern California. ADNI data are disseminated by the Laboratory for Neuro Imaging at the University of Southern California.

Appendix A. Supplementary data

Supplementary data associated with this article can be found, in the online version, at https://doi.org/10.1016/j.artmed.2020.101940.

References

[1] Wu X, Li J, Ayutyanont N, et al. The receiver operational characteristic for binary classification with multiple indices and its application to the neuroimaging study of Alzheimer's disease. IEEE/ACM Trans Comput Biol Bioinf 2013;10(1):173–80.
[2] Zhang F, Tian S, Chen S, et al. Voxel-based morphometry: improving the diagnosis of Alzheimer's disease based on an extreme learning machine method from the ADNI cohort. Neuroscience 2019;414:273–9.
[3] Álvarez Illán I, Górriz JM, Ramírez J, et al. An optimal decisional space for the classification of Alzheimer's disease and mild cognitive impairment. IEEE Trans Biomed Eng 2014;68(8):2245–53.
[4] Carrillo MC, Bain LJ, Frisoni GB. Worldwide Alzheimer's disease neuroimaging initiative. Alzheimer's Dement 2012;8(4):337–42.
[5] Kadmiri NE, Said N, Slassi I, et al. Biomarkers for Alzheimer disease: classical and novel candidates' review. Neuroscience 2018;370:181–90.
[6] Ashburner J, Friston KJ. Voxel-based morphometry-the methods. Neuroimage 2000;11(6):805–21.
[7] Korábečný J, Nepovimová E, Cikánková T, et al. Newly developed drugs for Alzheimer's disease in relation to energy metabolism, cholinergic and monoaminergic neurotransmission. Neuroscience 2018;370:191–206.
[8] H. Li, M. Habes, D.A. Wolk, et al., A deep learning model for early prediction of Alzheimer's disease dementia based on hippocampal MRI, ArXiv abs/1904.07282.
[9] Hao X, Li C, Yan J, et al. Identification of associations between genotypes and longitudinal phenotypes via temporally-constrained group sparse canonical correlation analysis. Bioinformatics 2017;33(14):i341–9.
[10] Masscli D, DiNuzzo M, Serra L, et al. Disruption of semantic network in mild Alzheimer's disease revealed by resting-state fMRI. Neuroscience 2018;371:38–48.
[11] Leung KK, Barnes J, Modat M, et al. Brain MAPS: an automated, accurate and robust brain extraction technique using a template library. Neuroimage 2011;55(3):1091–108.
[12] Behrmann J, Etmann C, Boskamp T. Deep learning for tumor classification in imaging mass spectrometry. Bioinformatics 2017;34(7):1215–23.
[13] Wan M, Gu G, Sun J. A level set method for infrared image segmentation using global and local information. Remote Sens 2018;10(7):1039–75.
[14] Feng J, Liu X, Dong Y, et al. Structural difference histogram representation for texture image classification. IET Image Process 2016;11(2):118–25.
[15] Zhang F, Li Z, Zhang B, et al. Multi-modal deep learning model for auxiliary diagnosis of Alzheimer's disease. Neurocomputing 2019;361:185–95.
[16] Greenlaw K, Szefer E, Graham J, et al. A Bayesian group sparse multi-task regression model for imaging genetics. Bioinformatics 2017;33(16):2513–22.
[17] Casanova R, Wagner B, Whitlow CT, et al. High dimensional classification of structural MRI Alzheimer's disease data based on large scale regularization. Front Neuroinform 2011;5:22–30.
[18] Misra C, Fan Y, Davatzikos C. Baseline and longitudinal patterns of brain atrophy in MCI patients, and their use in prediction of short-term conversion to AD: results from ADNI. Neuroimage 2009;44(4):1415–42.
[19] Zhang D, Wang Y, Zhou L, et al. Multimodal classification of Alzheimer's disease and mild cognitive impairment. Neuroimage 2011;55(3):856–67.
[20] Liu S, Liu S, Cai W, et al. Multimodal neuroimaging feature learning for multiclass diagnosis of Alzheimer's disease. IEEE Trans Biomed Eng 2015;62(4):1132–40.
[21] Li J, Gong Y, Tang X. Hierarchical subcortical sub-regional shape network analysis in Alzheimer's disease. Neuroscience 2017;366:70–83.
[22] Magnin B, Mesrob L, hun SK. Support vector machine-based classification of Alzheimer's disease from whole-brain anatomical MRI. Neuroradiology 2009;51(2):73–83.
[23] Zhang J, Yu C, Jiang G, et al. 3D texture analysis on MRI images of Alzheimer's disease. Brain Imag Behav 2012;6(1):61–9.
[24] Pachauri D, Hinrichs C, Chung MK, et al. Topology-based kernels with application to inference problems in Alzheimer's disease. IEEE Trans Med Imag 2017;30(10):1760–70.
[25] Lei B, Yang P, Wang T, et al. Relational-regularized discriminative sparse learning for Alzheimer's disease diagnosis. IEEE Trans Cybern 2017;47(4):1102–13.
[26] Dong Y, Feng J, Liang L, et al. Multiscale sampling based texture image classification. IEEE Signal Process Lett 2017;24(5):614–8.
[27] Zhang Y, Wang S, Phillips P, et al. Detection of Alzheimer's disease and mild cognitive impairment based on structural volumetric MR images using 3D-DWT and WTA-KSVM trained by PSOTVAC. BioMed Sign Process Contr 2015;21:58–73.
[28] Yang X, Tan MZ, Qiu A. CSF and brain structural imaging markers of the Alzheimer's pathological cascade. PLOS ONE 2012;7(12):e47406–12.
[29] Shen D, Davatzikos C. HAMMER: hierarchical attribute matching mechanism for elastic registration. IEEE Trans Med Imag 2002;21(11):1421–39.
[30] Mohammadi-Nejad AR, Hossein-Zadeh GA, Soltanian H, et al. Structured and sparse canonical correlation analysis as a brain-wide multi-modal data fusion approach. IEEE Trans Med Imag 2017;36(7):1438–48.
[31] Sherbet GV, Woo WL, Dlay SS. Application of artificial intelligence-based technology in cancer management: a commentary on the deployment of artificial neural networks. Anticancer Res 2018;38(12):6607–13.
[32] Nalepa J, Lorenzo PR, Marcinkiewicz M, et al. Fully-automated deep learning-powered system for DCE-MRI analysis of brain tumors. Artif Intell Med 2020;102:101769.
[33] Sengupta S, Singh A, Leopold HA, et al. Ophthalmic diagnosis using deep learning with fundus images – a critical review. Artif Intell Med 2020;102:101758.
[34] Arifoglu D, Bouchachia A. Detection of abnormal behaviour for dementia sufferers using convolutional neural networks. Artif Intell Med 2019;94:88–95.
[35] Bernal J, Kushibar K, Asfaw DS, et al. Deep convolutional neural networks for brain image analysis on magnetic resonance imaging: a review. Artif Intell Med 2019;95:64–81.
[36] Lamy JB, Sekar B, Guezennec G, et al. Explainable artificial intelligence for breast cancer: a visual case-based reasoning approach. Artif Intell Med 2019;94:42–53.
[37] Li X, Shen L, Xie X, et al. Multi-resolution convolutional networks for chest X-ray radiograph based lung nodule detection. Artif Intell Med 2020;103:101744.
[38] Chupin M, Gérardin E, Cuingnet R, et al. Fully automatic hippocampus segmentation and classification in Alzheimer's disease and mild cognitive impairment applied on data from ADNI. Hippocampus 2009;19(6):579–87.
[39] Dukart J, Kherif F, Mueller K, et al. Generative FDG-PET and MRI model of aging and disease progression in Alzheimer's disease. PLoS Comput Biol 2013;9(4):e1002987–97.
[40] López M, Ramírez J, Górriz JM. Principal component analysis-based techniques and supervised classification schemes for the early detection of Alzheimer's disease. Neurocomputing 2011;74(8):1260–71.
[41] Gray KR, Aljabar P, Heckemann RA, et al. Random forest-based similarity measures for multi-modal classification of Alzheimer's disease. Neuroimage 2013;65:167–75.
[42] Novellino F, Vasta R, Sarica A, et al. Relationship between hippocampal subfields and category cued recall in AD and PDD: a multimodal MRI study. Neuroscience 2018;371:506–17.

[43] Cuingnet R, Gerardin E, Tessieras J, et al. Automatic classification of patients with Alzheimer's disease from structural MRI: a comparison of ten methods using the ADNI database. Neuroimage 2011;56(2):766–81.
[44] Salas-Gonzalez D, Górriz D, Ramírez J. Feature selection using factor analysis for Alzheimer's diagnosis using PET images. Med Phys 2010;37(11):6084–95.
[45] Jack CR, Petersen RC, Xu YC, et al. Medial temporal atrophy on MRI in normal aging and very mild Alzheimer's disease. Neurology 1997;49(3):786–94.
[46] Suk HI, Lee SW, Shen D, et al. Hierarchical feature representation and multimodal fusion with deep learning for AD/MCI diagnosis. Neuroimage 2014;101:569–82.
[47] Xia H, Hoi SCH. Mkboost: a framework of multiple kernel boosting. IEEE Trans Knowl Data Eng 2013;25(7):1574–86.
[48] Gray KR, Wolz R, Hekemann RA, et al. Multi-region analysis of longitudinal FDG-PET for the classification of Alzheimer's disease. Neuroimage 2012;60(1):221–9.
[49] Ahmed OB, Benois-Pineau J, Allard M, et al. Classification of Alzheimer's disease subjects from MRI using hippocampal visual features. Multimed Tools Appl 2015;74(4):1249–66.
[50] Khedher L, Ramírez J, Górriz JM. Early diagnosis of Alzheimer's disease based on partial least squares, principal component analysis and support vector machine using segmented MRI images. Neurocomputing 2015;151:139–50.
[51] Liu J, Li M, Lan W, et al. Classification of Alzheimer's disease using whole brain hierarchical network. IEEE/ACM Trans Comput Biol Bioinf 2018;55(2):624–32.
[52] Ju R, Li C. Early diagnosis of Alzheimer's disease based on resting-state brain networks and deep learning. IEEE/ACM Trans Comput Biol Bioinf 2018;16(1):244–57.
[53] Chen G, Ward BD, Xie C, et al. Classification of Alzheimer disease, mild cognitive impairment, and normal cognitive status with large-scale network analysis based on resting-state functional MR imaging. Radiology 2011;259(1):213–21.
[54] Wee CY, Yap PT, Denny K, et al. Resting-state multi-spectrum functional connectivity networks for identification of MCI patients. PLoS ONE 2012;7(5):e37828–38.
[55] Li Y, Wang Y, Wu G, et al. Discriminant analysis of longitudinal cortical thickness changes in Alzheimer's disease using dynamic and network features. Neurobiol Aging 2012;33(2). pp. 427.e15–427.e30.
[56] Cho Y, Seong JK, Jeong Y, et al. Individual subject classification for Alzheimer's disease based on incremental learning using a spatial frequency representation of cortical thickness data. Neuroimage 2012;59(3):2217–30.
[57] He Y, Chen Z, Evans A. Structural insights into aberrant topological patterns of large-scale cortical networks in Alzheimer's disease. J Neurosci 2008;28(18):4756–66.
[58] Dai D, He H, Vogelstein JT, et al. Accurate prediction of AD patients using cortical thickness networks. Mach Vis Appl 2013;24(7):1445–57.
[59] Jha D, Alam S, Pyun JY, et al. Alzheimer's disease detection using extreme learning machine, complex dual tree wavelet principal coefficients and linear discriminant analysis, J. Med Imag Health Inf 2018;8(5):881–90.
[60] Zhang Y, Wang S, Sui Y, et al. Multivariate approach for Alzheimer's disease detection using stationary wavelet entropy and predator-prey particle swarm optimization. J Alzheimer's Dis 2018;65(3):855–69.
[61] Bendib MM, Merouani HF, Diaba F. Automatic segmentation of brain MRI through stationary wavelet transform and random forests. Pattern Anal Appl 2014;17(2):829–43.
[62] Rafiee G, Dlay SS, Woo WL. Region-of-interest extraction in low depth of field images using ensemble clustering and difference of Gaussian approaches. Pattern Recognit 2013;46:2685–99.
[63] J. Ashburner, T. Group, Statistical parametric mapping (SPM8), Functional Imaging Laboratory, Institute of Neurology 12, Queen Square, London WC1N 3BG, UK.
[64] Tzourio-Mazoyer N, Landeau B, Papathanassiou D, Crivello F, Etard O, Delcroix N, et al. Automated anatomical labeling of activations in spm using a macroscopic anatomical parcellation of the mni mri single-subject brain. Neuroimage 2002;15(1):273–89.
[65] Fung G, Stoeckel J. SVM feature selection for classification of SPECT images of Alzheimer's disease using spatial information. Knowl Inf Syst 2007;11(2):243–58.
[66] Liu M, Zhang J, Nie D. Anatomical landmark based deep feature representation for MR images in brain disease diagnosis. IEEE J Biomed Health Inf 2018;22(5):1476–85.
[67] Liu X, Wang Y, Ji H, Aihara K, Chen L. Personalized characterization of diseases using sample-specific networks. Nucleic Acids Res 2016;44(22):e164–74.
[68] Liu R, Chen P, Chen L. Detection for disease tipping points by landscape dynamic network biomarkers. Natl Sci Rev 2019;6:775–85.